Electronic Supplementary Material (ESI) for Journal of Materials Chemistry C.
This journal is © The Royal Society of Chemistry 2024

Supporting Information

Using Spatial Confinement to Decipher Polymorphism in the Organic Semiconductor p-DTS(FBTTh$_2$)$_2$

Sara Marina[1], Matthew Dyson[2], Xabier Rodríguez-Martínez[3], Obadiah G. Reid[4,5], Ruipeng Li[6], Garry Rumbles[4], Detlef Smilgies[6], Aram Amassian[7], Mariano Campoy-Quiles[3], Natalie Stingelin[8]*, Jaime Martín[1,9]*

[1] POLYMAT, University of the Basque Country UPV/EHU Av. de Tolosa 72, 20018, San Sebastián, Spain
[2] Imperial College London, Exhibition Road, London SW7 2AZ, UK
[3] Institut de Ciència de Materials de Barcelona, ICMAB-CSIC, Campus UAB, 08193, Bellaterra, Spain
[4] Chemical and Materials Science Center, National Renewable Energy Laboratory, 15013 Denver West Parkway, Golden, Colorado 80401, USA
[5] Renewable and Sustainable Energy Institute, University of Colorado Boulder
4001 Discovery Drive, Boulder, CO 80303, USA
[6] Cornell High Energy Synchrotron Source, Wilson Laboratory, Cornell University, Ithaca, New York 14853, USA
[7] Materials Science and Engineering, North Carolina State University, Raleigh NC 27695, USA
[8] School of Materials Science and Engineering and School of Chemical & Biomolecular Engineering, Georgia Institute of Technology, 311 Ferst Drive, Atlanta, Georgia, 30332, USA
[9] Universidade da Coruña, Campus Industrial de Ferrol, CITENI, Esteiro, 15471 Ferrol, Spain.

E-mail: jaime.martin.perez@udc.es, natalie.stingelin@gatech.edu

Experimental details

Materials.

p-DTS $(FBTTh_2)_2$ was obtained from 1Materials, Canada, and was used without further purification.

Nanoporous anodic aluminum oxide (AAO) mebranes with pore diameters of 25 nm, 40 nm, 60 nm, 180 nm and 400 nm, and a pore depth of 100 μm were purchased from SmartMembranes GmH (Germany).

Sample preparation.

Nanoporous AAO templates were first sonicated in hexane, acetone, isopropanol and water to remove organic molecules attached to the pore walls, which decrease their surface energy. p-DTS$(FBTTh_2)_2$ molecules were then infiltrated into the pores by melting p-DTS$(FBTTh_2)_2$ at 240 ºC on the surface of the AAO matrices. Due to the strong surface energy difference between the liquid organic compound and the hydroxylated pore walls of AAO templates, a spontaneous flow of p-DTS$(FBTTh_2)_2$ occurs along the nanopores. After 10 min, samples were cooled down to room temperature at 20 ºC/min. Finally, the residual *p*-DTS $(FBTTh_2)_2$ located on top of the AAO templates was removed with a sharp blade and a soft tissue so that the *p*-DTS $(FBTTh_2)_2$ within the AAO were isolated entities separated from each other.

Scanning electron microscopy (SEM)

Morphology of AAO templates was analyzed using a Hitachi SU8000 microscope with 0.5 kV accelerating voltage

Differential Scanning Calorimetry (DSC)

Thermal characterization of the samples was conducted by differential scanning calorimetry (DSC) (Mettler–Toledo DSC1 Star). Heating and cooling scans were performed at 20 ºC/min under constant flow of nitrogen. For the DSC study, the aluminum substrates attached to the AAO templates were selectively etched employing a mixture of 1.7 g CuCl2•H2O, 50 ml concentrated HCl and 50 ml deionized water.

Polarized Optical Microscopy (POM)

For the inspection of samples, both an Olympus BX51 microscope and a Zeiss Axio A-1 microscope were used in crossed nicols mode. The temperature during the experiments was controlled with a in a microscope hot stage (Linkam Scientific Instruments Ltd.).

Grazing Incidence X-Ray Scattering (GIWAXS)

GIWAXS experiments were conducted at D-line, Cornell High Energy Synchrotron Source (CHESS) at Cornell University (USA) as well as at the SAXS line of Elettra Sincrotrone (Italy). In general, X-ray beam was shone on the samples with incidence angles between above 1° so as to probe the material confined in the nanopores. The samples were placed in the set up so that the longitudinal axis of the nanopores were aligned with the vertical *z*-direction (see Figure S4 of the Supporting Information).

At CHESS, a X-ray beam with a wavelength of 1.155Å was used. A Pilatus 200k detector with a pixel size of 172μm was placed at a distance of 16.5 cm from the samples. A 1.5 mm wide molybdenum rod was used to block the intense scattering in the small-angle area. The exposure time measurements was 1s. For the temperature resolved WAXS

measurements, a hot stage with a water-cooled base was employed and a heating/cooling rate of approx. 40 °C/min was applied

At Elettra Sincrotrone a wide band-pass (1.47%) X-ray beam with a wavelength of 1.54 Å was used. A Pilatus 1M detector with a pixel size of 172μm was placed at a distance of 17.0 cm from the samples. The exposure time for room temperature measurements was 10s and the one for the temperature-resolved experiments was 1s. An Anton Paar hot stage was employed and heating and cooling rates of 40 °C/min were used.

Simulation of the GIWAXS pattern from phase II

GIWAXS pattern simulation was done employing the *indexGIXS* software [1] according to the lattice proposed by Love et al [2]. Once we checked that the patterns of phase I could be adequately simulated, the lattice parameters were modified until the generated pattern fitted the experimental pattern for phase II

Raman spectroscopy

Samples in the phase II were prepared as follows: p-DTS $(FBTTh_2)_2$ samples confined in 60 nm pores were first taken to a temperature above the melting of Phase II, e.g. 280ºC and then isothermically crystallized for 30 min at a temperature in between the crystallization temperature of phase II and the solid-solid transition, e.g. at 220ºC. Then samples were rapidly cooled down (quenched) in ice-water and stored at ambient temperature. The samples thus prepared exhibited solely the reflections of the phase II crystals.

Experimental Raman spectra were acquired in backscattering configuration in a WITec alpha300RA setup using a 488 nm solid-state laser as excitation source. An Olympus objective with 10X magnification (NA 0.25) was used to focus the incident laser and to collect the scattered light on-the-fly over 1 mm^2 areas. The laser intensity was lowered (ca. 2 mW) to avoid the rapid photodegradation of the sample and the integration times reduced (ca. 100 ms) to minimize the exposure time of the sample to the focused laser. The collected spectra were then averaged in each area to yield the representative vibrational fingerprint of the polymorphs. A 1200 grooves/mm grating coupled to a 1024 pixels Peltier-cooled charge-coupled device provided a spectral resolution of ca. 2 cm^{-1}.

For the simulation of the Raman spectra DFT calculations were performed using GAUSSIAN09 package at a B3LYP/6-31G(d) level of theory, which provides a great computational cost-performance balance. The calculations were performed on a single molecule in vacuum and at 298 K, including methyl-substituted side chains to reduce computational cost. All chemical structures and geometries were energetically optimized prior to calculation of the Raman-active normal modes and Raman activities. The convergence was accelerated by constraining the molecules to point group symmetries (either C_s or C_{2v}). Lorentzian line shapes of 8 cm^{-1} FWHM were used for the plots and their corresponding Raman intensities (I_i) were calculated for 488 nm excitation wavelength according to the classical theory of Raman scattering:[3]

$$I_i = \frac{S_i(\nu_0 - \nu_i)^4}{\nu_i\left[1 - \exp\left(-\frac{hc\nu_i}{k_B T}\right)\right]}$$

where ν_0 corresponds to the excitation frequency and ν_i is the ith vibrational frequency with Raman activity S_i. h, c, k_B and T correspond to the Planck's constant, the speed of light in vacuum, the Boltzmann's constant and the temperature, respectively. A uniform

scaling factor of 0.9614 was applied to the calculated frequencies to account for the anharmonicity of the normal vibrations and the deviations of the force fields.[4]

Photoluminescence spectroscopy (PL)

Photoluminescence (PL) spectra were acquired at room temperature (295 K) and 80 K using an Edinburgh Instruments FLSP920 double-monochromator spectrophotometer, equipped with a cooled NIR detector. Excitation was at 580 nm (2.14 eV) with a 10 nm bandwidth, emission was collected in 2 nm increments with a 4 nm bandwidth, and a 590 nm long-pass filter used to attenuate reflected incident light. To ensure an adequate signal to noise ratio light was collected for 1s at each emission wavelength, and then integrated over 10 scans. No PL emission was observed from unfilled porous Al substrates. Samples for PL were prepared as for Raman spectroscopy.

Time resolved microwave conductivity (TRMC)

TRMC experiments were conducted in an apparatus that has been thoroughly described.[5, 6] We measure the absorption of a microwave probe (~9 GHz) as a function of time after laser excitation, and use numerical simulations of the electromagnetic field distribution in the sample resonator to derive quantitative values for the photoconductance of the sample. In the present case a specialized microwave resonator was used that allows fragile free-standing samples to be sandwiched between a pair of identical quartz slides, the K-factor of which is 23,000. However, the samples were prepared on round alumina templates roughly 20 mm in diameter, and do not in general cover the entire area of the microwave waveguide cross section. They are cut in half, providing a roughly half-moon shape. We combine image analysis with our previous simulations of partial sample

coverage to correct the K-factor uniquely for each sample.[5] Samples for TRMC were prepared as for Raman spectroscopy.

Absorption Spectroscopy

Determining the absorption spectrum of confined small molecules is non-trivial since the nanoporous matrix hinders conventional transmission-based methods. As such, we turn to photothermal deflection spectroscopy (PDS), which instead relies on absorption induced heating to deflect a laser passing parallel to the substrate. This method cannot provide absolute values of the absorption coefficient, since the signal is usually scaled to overlap with values calculated from transmission and reflection spectra;[7, 8] furthermore, the PDS signal is only change linearly with absorption below the main absorption band. Despite these substantial caveats, PDS spectra nonetheless facilitate comparison between absorption by the two confined T1 polymorphs.

PDS was performed by suspending an aluminium substrate with T1 filled nanopores in perfluorohexane (Fluorinert FC-72, Sigma-Aldrich) and irradiating with monochromatic light (Newport Cornerstone 260, bandwidth 20 nm), modulated at 4 Hz (various low-pass filters attenuate unwanted harmonics). Absorption heats the adjacent liquid, producing a refractive index gradient that deflects a parallel and adjacent 633 nm HeNe laser. At small absorption/deflections absorption is considered proportional to the deflection signal at a quadrant detector (Thorlabs PDQ80A) 2 m from the sample, extracted using a lock-in amplifier (Stanford SR830). Finally, this signal is divided by incident intensity (determined from calibrated Si and InGaAs photodiodes). Note that no PDS signal is obtained from an aluminium substrate with empty pores, and that while reflection from aluminium increases the optical path length (and hence absorption), the increase from ~

85 to 100 % reflection above 1.3 eV (900 nm) is substantially smaller than the increase in Urbach energy relative to unconfined conjugated molecules.

Samples for PDS were prepared as for Raman spectroscopy.

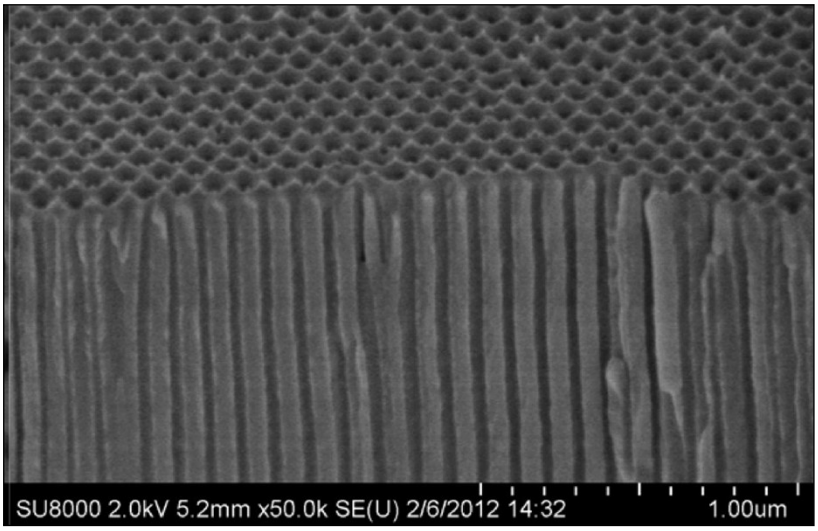

Figure S1. Cross-sectional view of a AAO with pores of 40 nm in diameter.

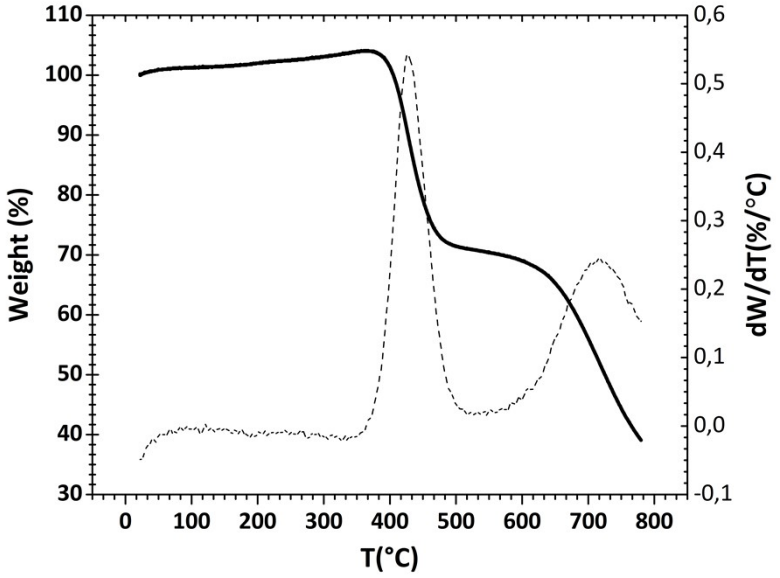

Figure S2. Thermogravimetric analysis (TGA) of p-DTS(FBTTh$_2$)$_2$, showing that no degradation occurs in the temperature range analyzed.

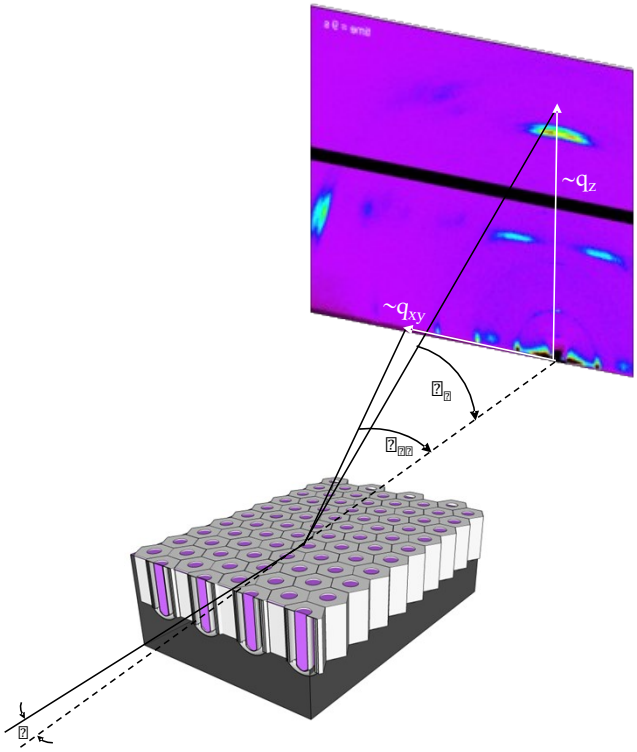

Figure S3. Schematic of experimental geometry used for GIWAXS characterization.

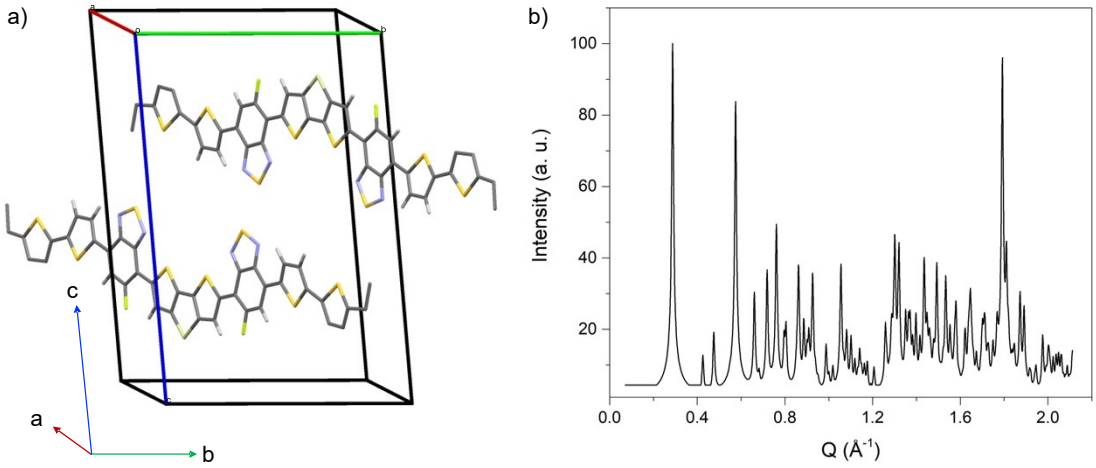

Figure S4. (a) Triclinic unit cell of *p*-DTS(FBTTh$_2$)$_2$ phase I and (b) theoretical powder diffractogram (calculated with *Mercury 3.8* software).

The unit cell determined for *p*-DTS(FBTTh$_2$)$_2$ has two molecules in triclinic symmetry as depicted in Fig. S7. In this lattice, the π - π stacking occurs along the <141> crystallographic direction. Orthogonally to this, the molecules pack in alternating stacks of aromatic backbones and ethyl hexyl side chains of the dithienosilole unit along the <001> crystallographic direction. This cell fundamentally agrees with the that by Love et al. for *p*-DTS(FBTTh$_2$)$_2$ single crystals.[2]

Figure S5. Polarized optical microscopy images of the surface of a 60 nm AAO infiltrated with p-DTS $(FBTTh_2)_2$ acquired during heating from 30 to 280 ºC at 4 °C min^{-1}. The temperatures at which the images were acquired are indicated in the pictures. Lateral size of each picture is 100 μm.

Further evidences of a complex thermal behavior of p-DTS$(FBTTh_2)_2$ under strong spatial confinement was obtained by polarized optical microscopy, POM. In the experiment presented in Figure 1b, images were acquired in reflection mode while heating up a freshly prepared 60 nm sample from 30 ºC to 280 ºC at 4 °C min^{-1}. The experiment is thus comparable to the 1st heating DSC scan. Indeed, like in the DSC 1st heating scan, the melting of phase I crystals was detected, here as a loss of the material´s birefringence, at around 200 ºC. Interestingly, the birefringence was again recovered upon further heating at 220 ºC, indicating the formation of a new high-temperature ordered structure, which melts at 260 ºC, i.e. at the temperature of the main endothermic peak in the DSC 2nd heating scan.

Discussion about the kinetic aspects of enantiotropic transition

Hence, because we identified a reversible solid-solid transition we advocate that phase I and phase II are enantiotropically related, i.e. that both of them are thermodynamically stable in their respective temperature ranges. However, DSC (Figure 2a) and the POM

(Figure S6) experiments do not seem to support that interpretation. In order to rationalize this, we must bring into the discussion the concept of the kinetic irreversibility of enantiotropic transitions,[9] which refers to the fact that although enantiotropic solid-solid transitions are, by definition, reversible and exhibit well-defined transition temperatures, transitions can or cannot be experimentally observed in practice. Even if a certain transition is thermodynamically possible, it can be effectively suppressed (during heating or cooling) if the energy barrier that must be overcome to alter the crystal structure is sufficiently high.

In addition to the above, an intermediate situation exists between total reversibility and total irreversibility, in which the polymorphic transition is not fully suppressed but it does not occur at the temperature marked by thermodynamics (during a heating/cooling ramp). In such a case, the energy barrier for the modification of the crystalline lattice introduces a "kinetic factor" and the observed solid-solid transition temperature becomes dependent on the kinetic aspects of the experiment itself, for example, on the heating and cooling rates applied. As a result, the transition is effectively shifted in temperature (in a heating/cooling) ramp or simply occurs after long times. We argue that the transition between phase I and phase II in p-DTS(FBTTh$_2$)$_2$ belong in this case, i.e. it is a kinetically hindered enantiotropic transition. This conclusion is furthermore supported by the results included in Figure S8 of the Supporting Information, which demonstrate that even if the polymorphic transition from phase II to phase I does not develop during the applied cooling ramp, it does occurs in the course of several days. (The discussion of the DSC and POM results in the frame of a kinetically hindered enantiotropic transition are included in the Supporting Information Figure S9.)

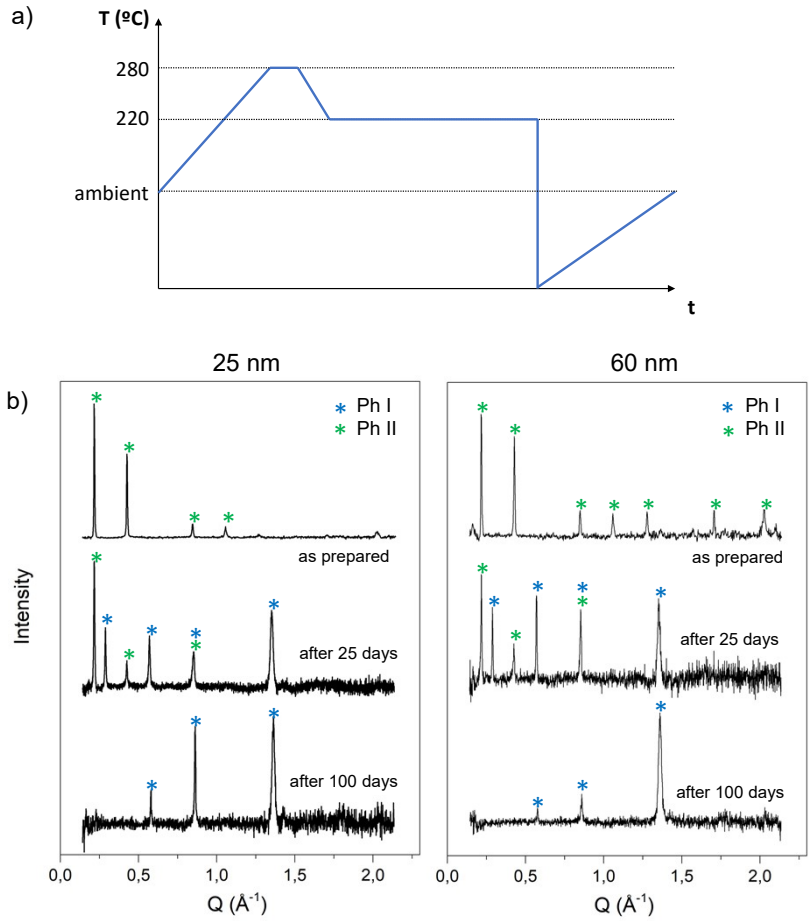

Figure S6. (a)Thermal history applied to samples in order to kinetically stabilize phase II crystals at ambien temperature. (b) Time evolution of the WAXS patterns for 25 and 60 nm p-DTS(FBTTh$_2$)$_2$ samples crystallized into the phase II during storage at ambient temperature.

In order to further prove that phase I and phase II are enatiotropically related but the transition is subject to a certain degree of kinetic irreversibility we conducted the following experiment: With the guidance of the phase diagram presented in figure 4b, we designed a thermal treatment that led to p-DTS(FBTTh$_2$)$_2$ samples crystallized exclusively into the phase II (Figure S7a). More specifically, 25 and 60 nm p-DTS(FBTTh$_2$)$_2$ samples were first taken to a temperature above the melting of Phase II, e.g. 280ºC and then isothermically crystallized for 30 min at a temperature in between the crystallization temperature of phase II and the solid-solid transition, e.g. at 220ºC (Figure S7a). Then samples were rapidly cooled down (quenched) in ice-water and stored at ambient temperature. The samples thus prepared exhibited solely the reflections of the phase II crystals, as can be seen in the WAXS pattern of figure S7b (upper lines in both panels), demonstrating the possibility of achieving p-DTS(FBTTh$_2$)$_2$ crystallized exclusively into the phase II at ambient temperature (as a metastable form). This is allowed because of the kinetic hinderance of this polymorphic

transition, which avoids the solid-solid transition to occur during the rapid cooling from the phase II region to the phase I region (figure 4a).

However, if this solid-solid transition is enantiotropic (and kinetically hindered but non-impeded) phase II crystals should eventually turn into phase I crystals because the thermodynamic phase at ambient temperature is phase I. Thus, we monitored the structure of the sample above over time. Figure 5 clearly shows how the WAXS pattern recorded after 25 days (from the preparation of samples) contains reflections from both phase I and phase II, whereas after 100 days, just reflections from phase I show up in the diffractogram, indicating that the conversion of phase II into phase I is completed.

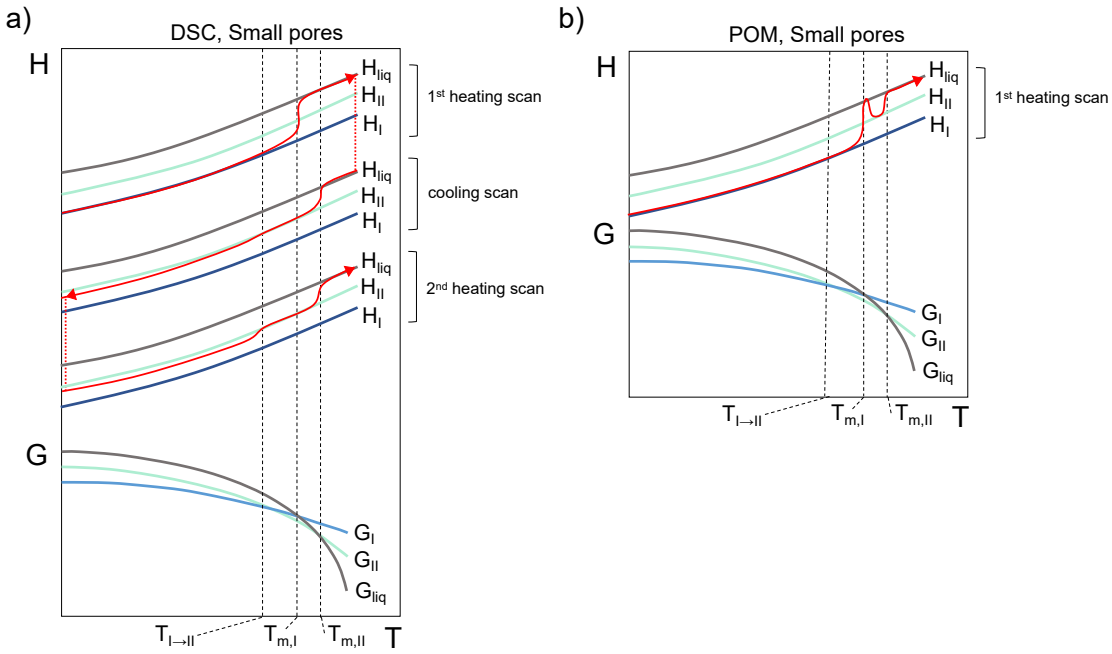

Figure S7. Thermodynamic picture (enthalpy *vs* T diagram) during the DSC scans (a) ad the POM scan (b) according to the proposed phase diagram

Let us now discuss our experiments in the frame of a kinetically hindered enantiotropic phase transition: Due to the relatively fast scanning rate applied in the DSC heating scans, i.e. 20 ºC min^{-1}, the kinetic hinderance for the solid-solid transition (and the formation of phase II in general) avoids the formation of phase II crystals neither in the DSC 1st heating trace nor in the cooling trace. In the POM heating scan, however, which is conducted at a slower rate (4 ºC min^{-1}), we do observe the formation of phase II crystals, but solely above the melting of phase II; hence, far above the thermodynamic transition temperature. Lastly, in the GIWAXS experiments, where the scanning rate was approx. 20 ºC min^{-1}, we observe a partial solid-solid transformation during both the heating (before the melting phase I) and the cooling ramps, but this is simply because this technique has demonstrated to be far more sensitivity than the techniques above to probe crystal structures. In summary, all our experimental findings can be rationalized

in terms of an enantiotropic transition that is subject to a certain degree of kinetic irreversibility. For a further thermodynamic description of the DSC and POM experiments see the schematic enthalpy *vs* T diagrams provided in the figure S9.

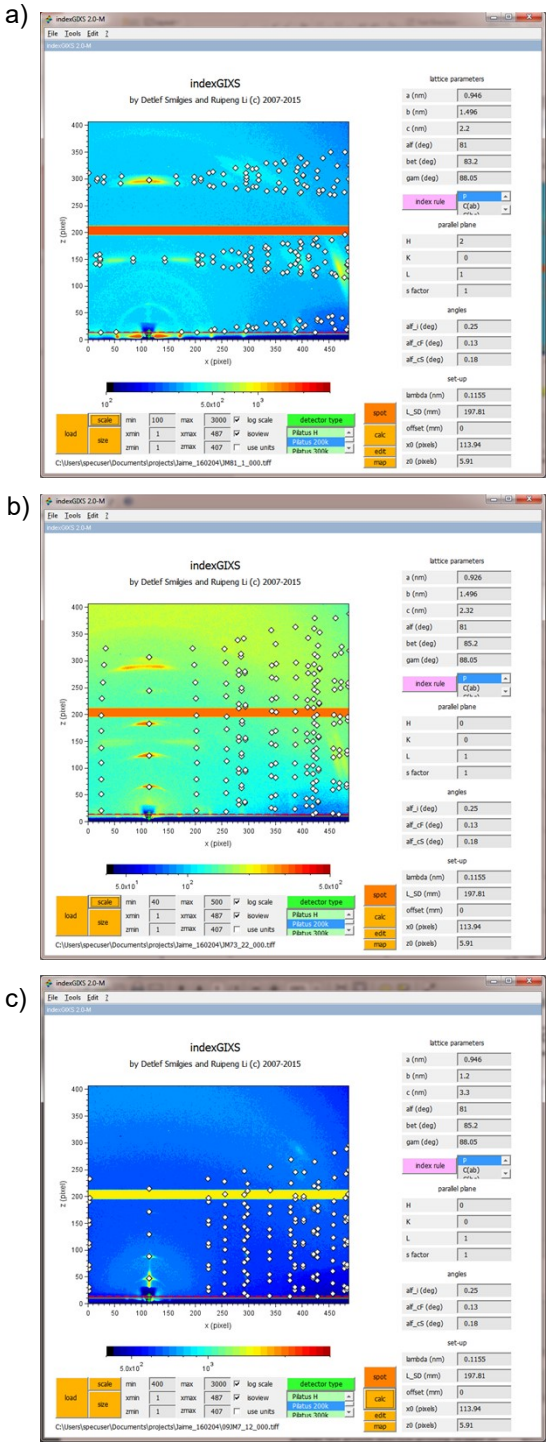

Figure S8. Indexation of 2D GIWAXS patterns for crystal phases I and II with the [2]. (a) Indexation of Phase I lattice with (201) orientation ((201) planes perpendicular to the vertical axis) and (b) with (001) orientation ((001) planes perpendicular to the vertical axis). (c) Indexation of Phase I lattice with (001)* orientation ((001)* planes perpendicular to the vertical axis)

Motivated by the similarity of the patterns from phase I and phase II, we tried to gain information about the crystal lattice of phase II from that of phase I as follows: We began simulating the pattern of phase I employing the *indexGIXS* software [1] according to the lattice proposed by Love et al [2] (figures S9a and S9b). Once we checked that the patterns of phase I could be adequately simulated, the lattice parameters were modified until the generated pattern fitted the experimental pattern for phase II

Phase I	Phase II
Triclinic unit cell a: 0.95 nm b: 1.50 c: 2.2 nm α: 81 º β: 83.2º γ:88.05	Triclinic unit cell a: 0.95 nm b: 1.20 c: 3.3 nm α: 81 º β: 85.2º γ:88.05

We must note that because the analyzed GIWAXS pattern for phase II was acquired at elevated temperatures (220 ºC), some thermal expansion is expected in the crystal lattice analyzed, which should be reflected in the provided lattice parameters.

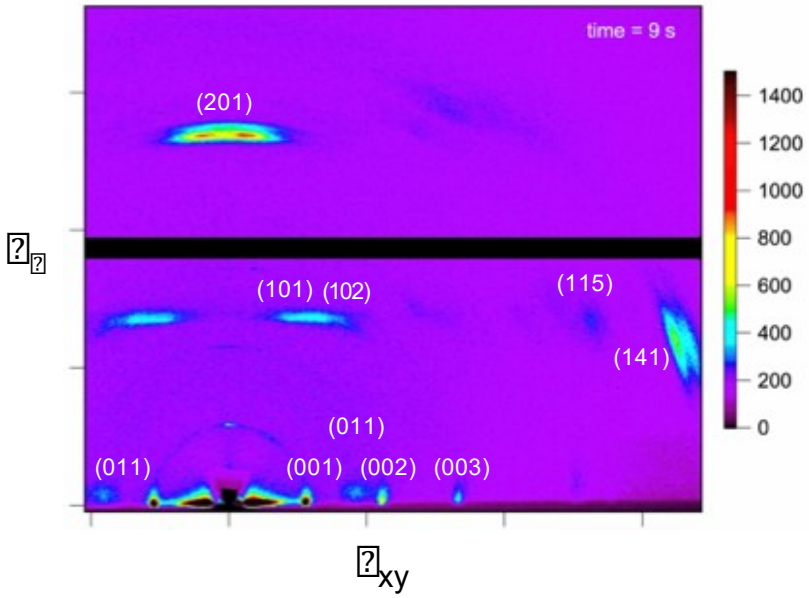

Figure S9. 2D GIWAXS pattern and peak indexation for phase I crystals

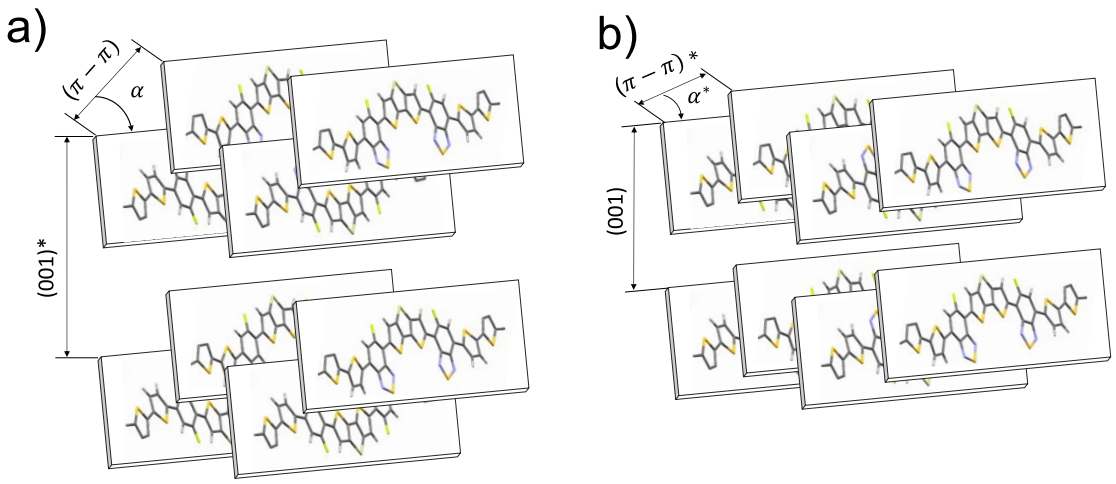

Figure S10. (a) and (b) are schematics of the molecular arrangements in phase II and phase I, respectively (alkyl chains have been omitted for clarity).

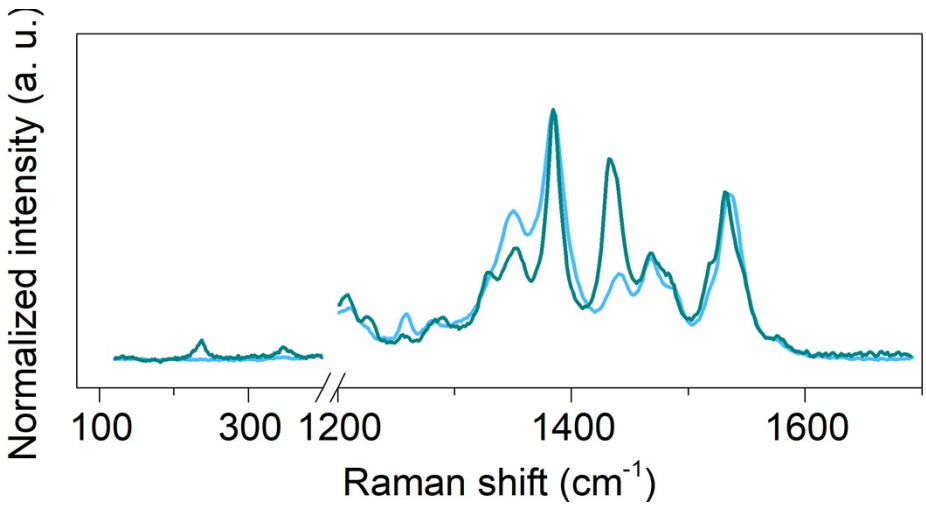

Figure S11. Raman spectra measured at 488 nm excitation for the two different p-DTS(FBTTh$_2$)$_2$ phases found experimentally. Arrows mark the bands where major differences between phase I and phase II are seen. (The thermal history applied to achieve phase II is described in the experimental part and in Figure S8a of the Supporting Information).

Further information about the molecular arrangement in phase II crystals was obtained from Raman spectroscopy. The experimental Raman spectra for 60-nm-in-diameter samples, shown in figure 5b of the manuscript, clearly depict distinguishable vibrational fingerprints for phase I and phase II. The major differences at the moderate frequency regime (1000-1600 cm^{-1}) arise at the 1437 cm^{-1} band, corresponding to the C-C stretching

mode of the lateral thiophenes (T); the 1351 cm^{-1} band, which corresponds to the C=C and C=N stretching mode at the benzothiadiazole (BT) moieties; and the 1258 cm^{-1} band, assigned to the C-C stretching at the BT units as well as at the dithienosilole core. DFT calculations (Figure S12) also indicate that at the low frequency regime (200-500 cm^{-1}) the modes arising in phase II correspond to bending modes at the BT and T units. Following this assignment and the matching with the experimental spectra, phase I and phase II may differ in the conformation of the BT and T units in the crystalline packing of the p-DTS($FBTTh_2$)$_2$ molecules. More specifically, phase II should provide a larger room for the BT and T moieties to deform while improving the electron-phonon coupling.

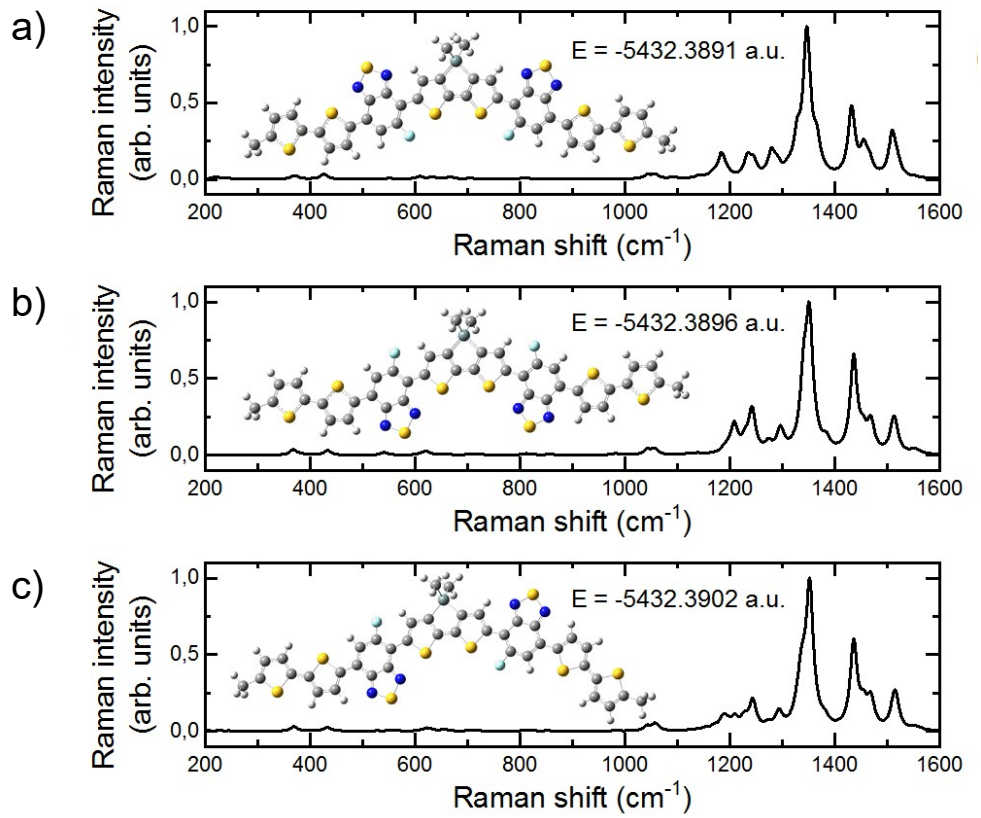

Figure S12. (a), (b) and (c) panels correspond to the DFT-simulated Raman intensity spectra of a single p-DTS($FBTTh_2$)$_2$ molecule in three different conformations, ordered from lower to higher stability as (a) < (b) < (c)

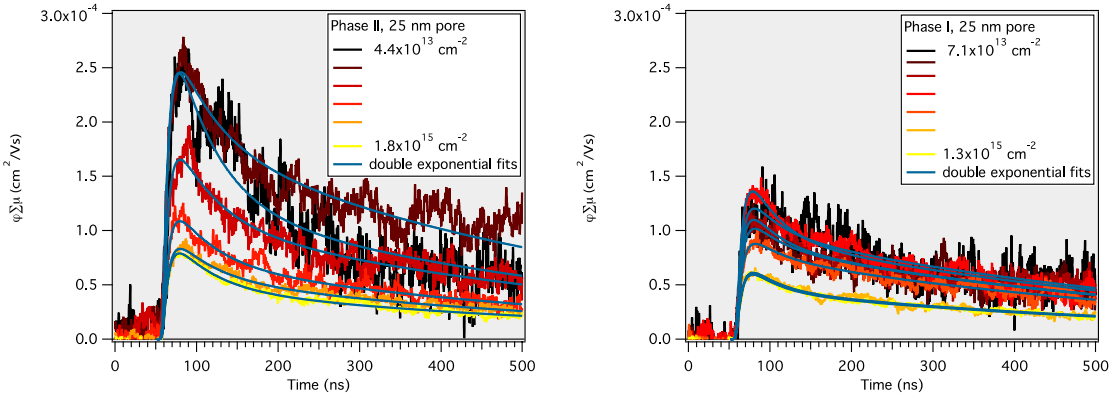

Figure S13. (a) and (b) show the microwave conductivity transients over two orders of magnitude in excitation fluence (500 nm pump), for phase II and phase I, respectively. Double exponential fits are displayed in blue. The y-axis is the yield-mobility product ($\varphi\Sigma\mu$)

References

1. Smilgies, D.-M.; A Blasini, D. R., Indexation scheme for oriented molecular thin films studied with grazing-incidence reciprocal-space mapping. *Journal of Applied Crystallography* **2007,** *40* (4), 716-718.
2. Love, J. A.; Proctor, C. M.; Liu, J.; Takacs, C. J.; Sharenko, A.; van der Poll, T. S.; Heeger, A. J.; Bazan, G. C.; Nguyen, T.-Q., Film Morphology of High Efficiency Solution-Processed Small-Molecule Solar Cells. *Advanced Functional Materials* **2013,** *23* (40), 5019-5026.
3. Krishnakumar, V.; Keresztury, G.; Sundius, T.; Ramasamy, R., Simulation of IR and Raman spectra based on scaled DFT force fields: a case study of 2-(methylthio)benzonitrile, with emphasis on band assignment. *Journal of Molecular Structure* **2004,** *702* (1), 9-21.
4. Scott, A. P.; Radom, L., Harmonic Vibrational Frequencies: An Evaluation of Hartree−Fock, Møller−Plesset, Quadratic Configuration Interaction, Density Functional Theory, and Semiempirical Scale Factors. *The Journal of Physical Chemistry* **1996,** *100* (41), 16502-16513.
5. Reid, O. G.; Moore, D. T.; Li, Z.; Zhao, D.; Yan, Y.; Zhu, K.; Rumbles, G., Quantitative analysis of time-resolved microwave conductivity data. *Journal of Physics D: Applied Physics* **2017,** *50* (49), 493002.
6. Savenije, T. J.; Ferguson, A. J.; Kopidakis, N.; Rumbles, G., Revealing the Dynamics of Charge Carriers in Polymer:Fullerene Blends Using Photoinduced Time-Resolved Microwave Conductivity. *The Journal of Physical Chemistry C* **2013,** *117* (46), 24085-24103.
7. Kronemeijer, A. J.; Pecunia, V.; Venkateshvaran, D.; Nikolka, M.; Sadhanala, A.; Moriarty, J.; Szumilo, M.; Sirringhaus, H., Two-Dimensional Carrier Distribution in Top-Gate Polymer Field-Effect Transistors: Correlation between Width of Density of Localized States and Urbach Energy. *Advanced Materials* **2014,** *26* (5), 728-733.

8. Venkateshvaran, D.; Nikolka, M.; Sadhanala, A.; Lemaur, V.; Zelazny, M.; Kepa, M.; Hurhangee, M.; Kronemeijer, A. J.; Pecunia, V.; Nasrallah, I.; Romanov, I.; Broch, K.; McCulloch, I.; Emin, D.; Olivier, Y.; Cornil, J.; Beljonne, D.; Sirringhaus, H., Approaching disorder-free transport in high-mobility conjugated polymers. *Nature* **2014,** *515* (7527), 384-388.
9. Kawakami, K., Reversibility of Enantiotropically Related Polymorphic Transformations from a Practical Viewpoint: Thermal Analysis of Kinetically Reversible/Irreversible Polymorphic Transformations. *Journal of Pharmaceutical Sciences* **2007,** *96* (5), 982-989.